

MA-SARNet: A One-Shot Forecasting Framework for SAR Image Prediction with Physical Driving Forces

Zhouyayan Li ^{a,b*}, Zhongrun Xiang ^c, Bekir Z. Demiray ^b, Muhammed Sit ^b, Ibrahim Demir ^{a,b,d}

^a Civil and Environmental Engineering, University of Iowa, Iowa City, Iowa, USA

^b IIHR Hydroscience and Engineering, University of Iowa, Iowa City, Iowa, USA

^c Capital One, McLean, Virginia, USA

^d Electrical and Computer Engineering, University of Iowa, Iowa City, Iowa, USA

* Corresponding Author, Email: zhouyayan-li@uiowa.edu

Abstract

Remote sensing imagery is one of the most widely used data sources for large-scale earth observations with consistent spatial and temporal quality. However, the current usage scenarios of remote sensing images are largely limited to retrospective tasks as they can only capture existing phenomena. This study proposes MA-SARNet, a one-shot forecasting framework built with a modified MA-Net structure and ResNet50 as the backbone, to predict the backscatter values of Synthetic-Aperture Radar (SAR) images using the previous observations, meteorological, and geomorphic data layers as input. The model was trained, validated, and tested with SAR images collected during the catastrophic 2019 Midwest U.S. Floods that affected several states on the Missouri and Mississippi River tributaries. Compared to the benchmark performance, model predictions show an increase of 31.9% and 17.8% for the mean and median AAI (Assemble Accuracy Index) and an increase of 37.9% and 15.1% for the mean and median NSE (Nash-Sutcliffe Efficiency) on the test set. Results showed that the flood extent derived from backscatter predictions is more robust against misclassifications caused by pixel-level noise compared to the flood map derived using the real backscatters and those from two additional flood map repositories. Results from spatial and temporal robustness tests demonstrate that the model has sufficient generalization potential for real-time, physically informed, deep learning-based earth surface prediction tasks to facilitate fast response to and mitigation for future floods.

Keywords: image synthesis, SAR, deep learning, floods, remote sensing

This manuscript is an EarthArXiv preprint and has been submitted for possible publication in a peer-reviewed journal. Subsequent versions of this manuscript may have slightly different content. Please feel free to contact the corresponding author for feedback.

1. Introduction

The 2019 Midwestern U.S. Floods, also known as the 2019 Floods in the Central U.S., consist of several historic flood events that occurred in the midwestern part of the US during the spring and summer of 2019. This flood series was observed mainly along the Missouri and Mississippi Rivers and had catastrophic influences on local communities in Nebraska, Iowa, Kansas, Missouri, and South Dakota, leading to an estimated economic loss of three billion USD (Flanagan et al., 2020; NASA 2022a). The flood series is believed to be attributable to a combination of excessive runoff caused by fast snow melt, the rain-on-snow process, and extreme precipitation from storms (Flanagan et al., 2020). Given the global climate change context, it is likely that some regions in the world will suffer from more frequent and severe floods (Hayhoe et al., 2018; Hammond et al., 2015; Haltas et al., 2021), causing significant impact on communities.

Remote-sensed images serve as an essential data source for earth observation and are widely used for flood extent mapping (Cherif et al., 2021; Dong et al., 2021; Moharrami et al., 2021; Dasgupta et al., 2022) and flood impact analysis (Xu et al., 2019). Among common types of remote sensing images, satellite images can provide large-scale observations with consistent quality and frequent revisit schedules (Tiwari et al., 2020; Choi et al., 2021), whereas aircraft imagery can provide very high resolution (VHR) images (Wang, Sun, et al., 2022; Wilson et al., 2022) with more flexibility and are thus ideal for local observing tasks. However, so far, most applications using remote sensing images are for retrospective rather than predictive tasks. This is because remote sensors can only capture surface characteristics that already exist. For instance, in order to extract flood extent from images captured by remote sensors, there must be inundation already occurring on the ground.

With the aim of expanding the application scenarios of remote sensing images into forecasting and flood preparedness tasks, we proposed a forecasting framework by analyzing the relationship between relevant physical driving forces and remote-sensed observations. Among all remote-sensed image types, we will be targeting the prediction of backscatter values of Synthetic-Aperture Radar (SAR) images for two main reasons. First, bands of a SAR image are more informative compared to bands of other widely used satellite image sources like Landsat and Sentinel-2 for flood extent delineation problems. Previous studies showed that the VV (vertical polarization transmitted, vertical polarization received) or VH (vertical polarization transmitted, horizontal polarization received) band of a SAR image on its own is sufficient for flood extent extraction (Twele et al., 2016; Manavalan et al., 2017; Markert et al., 2020; Tiwari et al., 2020) whereas it is more common to create a supplementary index (i.e., NDVI, NDWI) involving multiple bands for Landsat and Sentinel-2 images (Sivanpillai et al., 2021; Atefi and Miura 2022; Singh and Kansal 2022). It should be easier and more accurate for the model to learn a multi-to-one relationship (multiple input layers in, one output layer out) than a multi-to-multi (multiple input layers in, multiple output layers out) relationship with the same input. The other reason is that SAR detects with active rather than passive signals, which enables it to work both day and night independently from external illumination and weather conditions. This leads

to cloud-free scenes (ESA 2013) that avoid the common cloud-contamination issue on Landsat, Sentinel-2, and other optical images.

Recently, researchers have shown an increasing interest in applying state-of-the-art deep learning methods to single satellite images (Gautam et al., 2022) or image time series generation (Sit et al., 2021), image translation between different remote sensing data sources (Zhu and Kelly 2021; Vandal et al., 2022), and enhancing image resolution with deep-learning-based super-resolution techniques (Demiray et al., 2021a, Sit et al., 2022). Those studies have proven the efficacy of deep learning models in generating fake satellite image series or single images that are manually hard to distinguish from the target image. Based on those findings, advancements have been made in predicting meteorological variables such as precipitation (Amini et al., 2022; Ko et al., 2022); deriving secondary products such as land cover and vegetation conditions (Chowdhury et al., 2022; Kladny et al., 2022; Toker et al., 2022); and generating high spatial and temporal resolution images through image fusion that involves multiple image sources (Yang et al., 2021).

Despite all those advancements, most of those studies focused on the relationship between images corresponding to different time points within a certain period (image time series generation), the relationship between images coming from different sensors (image translation and image fusion), or the relationship between the image and its higher resolution version (image super resolution), for which the goal is to generate images that follow the same distribution as the target images and to maximize the structural similarity between the predicted image and the target (Demiray et al., 2021b). By contrast, for results to support flood preparedness and mitigation decisions (Ewing and Demir, 2021; Alabbad et al., 2022), it is more important for results to reflect the influence of physical driving forces on surface characteristics that are closely related to flood extent and other derived factors.

Requena-Mesa et al., (2021) introduced EarthNet2021, an image time series generation task that is aimed at forecasting Sentinel 2 image time series using time series of precipitation, sea level pressure, temperature, previous Sentinel 2 image series, and a fixed DEM layer as context. That one is, so far, the most relevant work to this study. However, the focus of their work is on introducing the EarthNet image dataset by proposing an image time series generation challenge, which has substantial differences from a one-shot prediction task. A time series generation task, for example, allows the output to learn from far more input information as well as previous output than a one-shot prediction task. In addition, many relevant studies did not include substantial discussion on how important or necessary each of those predictors was to help readers better understand the role of the meteorological and geomorphic driving forces the dataset contained.

The current work is, to the best of the authors' knowledge, the first study trying to build the relationship between various physical driving forces and the backscatter values of SAR images and to investigate the usefulness of those predictions on derived secondary products (i.e., flood extent). The main contributions to this work include the following: a) a one-shot forecasting framework connecting physical driving forces with the backscatter values on 10-m SAR images

is proposed for the first time in the literature; b) an in-depth investigation of the model's performance with different combinations of input data layers; c) qualitatively and quantitatively evaluating the model's performance on not only the predicted backscatter values but also investigating the quality of secondary products, such as flood extent maps, derived using those backscatter predictions; and d) investigating the model's temporal and spatial generalization power on images saved independently from the training, validation, and test sets. This study will help improve and streamline the application of SAR images in predictive tasks. Furthermore, this work will benefit relevant research topics such as radar-to-optical image translation, SAR-based data assimilation, image time series synthesis, and analysis by providing reliable SAR backscatter forecasting.

2. Data and Methodology

The SAR images used in this study come from Sentinel-1 satellites launched and maintained by the European Space Agency (ESA). Instead of processing the raw data from scratch, we used C-band Ground Range Detected (GRD) scenes readily available on Google Earth Engine (GEE). Those SAR images on GEE have gone through substantial preprocessing, such as orbit metadata update, thermal noise removal, and terrain correction (Moothedan et al., 2020), which therefore saved users a lot of effort for preprocessing.

As mentioned in the previous section, the 2019 Midwestern U.S. Floods contain several regional flood events happening in different parts of the central US throughout spring and summer, 2019. The affected area covers 55 HUC6 basins, which add up to an estimated 1,256,127 km². Due to the large spatial spread of the event and the 12-day revisit cycle of each of the two SENTINEL-1 satellites (two satellites in total), hundreds of SAR images were captured during the spring and summer of 2019 in those affected areas. To pinpoint the most relevant images, we first narrowed them down to the date when there were floods reported from the NASA Disasters Mapping Portal (NASA 2022b, 2022c), and then manually excluded the SAR images without noticeable changes compared to its dry conditions using the SAR-based Flood Inundation Archive, 2016-2019, created by Yang et al., (2021).

The abovementioned screening process helped us narrow the SAR collection down to 34 different SAR images. Among all these 34 SAR images, some of them have the same spatial coverage but were captured on different dates. We first saved two images, ending with the unique SAR image ID (ESA 2013) of 086E and 1544. Those two images do not overlap, or only overlap by a small portion, with any other images and will thus be used for the spatial robustness test. Then, we randomly selected 30 images out of the remaining 32 for model training, validation, and testing. The remaining two will be used for the temporal robustness test. In this study, the remaining two images for the temporal test are identified by IDs 8814 and 52FC. In short, the four images for the robustness test are saved separately from the 30 images used for training, validation, and testing. The difference between images for spatial and temporal tests is that some images in the training-validation-test collection may have the same spatial coverage as

images for temporal tests but were captured on different dates, but images for spatial tests will have no substantial overlapping with all the other images.

Typically, a single SAR image will contain several bands, including backscatters measured and received in different polarization combinations and a band of approximate incidence angle. To keep the problem doable, we selected the VV band of the target band to predict. The VV band is chosen because many previous studies reported the efficacy of this band over the VH band (Twele et al., 2016; Markert et al., 2020; Tiwari et al., 2020). Out of simplicity consideration, when we mentioned "SAR prediction" or "prediction" in all sections that follow, we were referring to the VV band of the SAR image. Figure 1 shows the study area represented with the SAR image coverage displayed with water body masks, with images for robustness tests marked with red and green inclined lines.

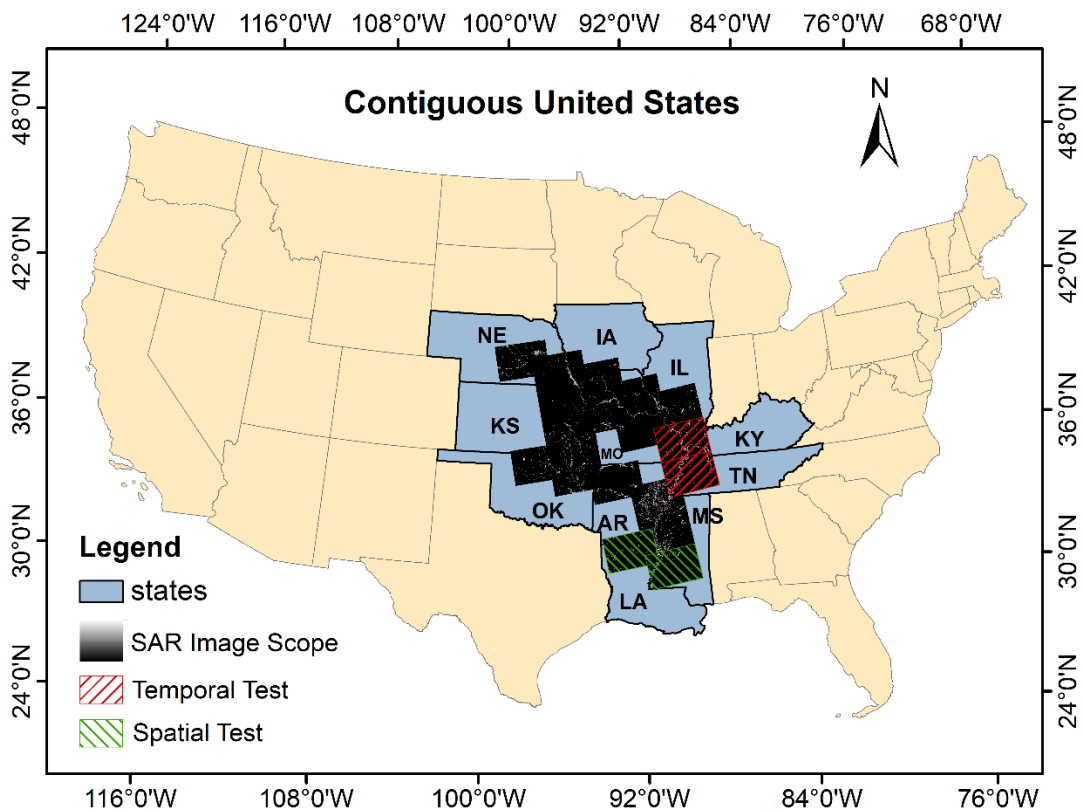


Figure 1. SAR scene scopes (displayed with water body masks) selected for model training, validation, and test, and those saved for model robustness test in this study

The geomorphic input considered in this study includes the Height Above Nearest Drainage (HAND) index and a land cover map. The HAND method is frequently used to predict flood inundation extents (Hu and Demir, 2021; Li et al., 2022) to support flood mitigation and impact analysis (Alabbad et al., 2021; Yildirim and Demir, 2022). HAND has been applied as a stand-alone flood mapping approach (Chaudhuri et al., 2021; Li and Demir, 2022a; Li et al., 2023), a supplementary dataset to refine the flood extent extracted from remotely sensed images (Zeng et

al., 2020; He et al., 2021; Li and Demir, 2022b), and an independent data layer in flood extent extraction with machine learning approaches (Aristizabal et al., 2020; Bosch et al., 2020; Esfandiari et al., 2020; Liu et al., 2020). The HAND layer comes from the 10 m HAND dataset for the continental United States (CONUS) created by Liu et al., (2016) and is organized by HUC6 basins. We downloaded those HAND files that share the same spatial coverage as the SAR images involved in this study. Then, we mosaiced those HAND patches to create one big patch that spatially covers all SAR images. The land cover map used in this study is the ESA WorldCover 10m v100 product provided by ESA for 2020 (Zanaga et al., 2021). The land cover map is created based on Sentinel-1 and Sentinel-2 data. We selected the WorldCover product out of many land cover map resources because of its high spatial resolution and consistency with SAR images. We anticipate that the surface grouping characteristics will be similar to those observed in 2019. This is justified because, normally, land cover changes much slower than meteorological factors like precipitation and is more expensive to collect and measure on a large scale. It is, therefore, very common that land cover maps, especially high-resolution products, are updated every few years instead of every year (Wickham et al., 2021). Since the HAND and land cover layers have the same spatial resolution as the SAR images, we simply clipped out the corresponding HAND and land cover patches using the extent of each SAR image and aligned the pixel centers of each input layer. The HAND and land cover layers will be referred to as L1 and L2, respectively.

The meteorological factors considered in this study include precipitation and soil moisture as they are closely related to the ground surface conditions during flood seasons and are therefore widely adopted in the literature for predicting earth surface observations (Requena-Mesa et al., 2021; Dasgupta et al., 2022; Diaconu et al., 2022). The precipitation used in this study is the Global Precipitation Measurement (GPM) v6 product coming from NASA GES DISC at NASA Goddard Space Flight Center with a recording frequency of every half an hour, a spatial resolution of 11,132 meters (about 0.1 degree), and worldwide coverage. Specifically, the calibrated snapshot precipitation (precipitationCal) is selected. We created five aggregations for the precipitation that occurred prior to the SAR capture date, namely, total precipitation over 24 hours, 25–48 hours, 49–72 hours, 73–120 hours, and 121–168 hours prior to the SAR capture timestamp. Here, the last two layers are aggregated over 48 hours instead of 24 hours because it is common that in hydro-science field, the current status is more sensitive to previous status or triggering factors that are temporally closer to the current one. We, therefore, believe it is acceptable to apply a coarse temporal aggregation scale for inputs that are further away from the current status. Admittedly, changing the temporal scales for precipitation aggregation could bring some uncertainties to the results, but this is an issue that is worth conducting an independent study on and thus falls outside the scope of the current work. These five accumulative precipitation layers will be referred to as L3 to L7.

We found that the practice of aggregating precipitation by day (Requena-Mesa et al., 2021; Diaconu et al., 2022) is problematic for SAR image synthesis. This is because ESA SAR images are usually captured within a short period of time and could happen very early in the morning,

such as at 12 a.m. In such cases, the majority of the precipitation on that specific day falls after the sensor finished capturing images, implying that the majority of the total precipitation on that day should be considered future data and should not be used to describe ground characteristics that occurred earlier.

The soil moisture data comes from the NASA-USDA enhanced SMAP dataset. This dataset comes with an averaged 3-day revisit frequency and a spatial resolution of 10 km. Specifically, the surface soil moisture (SSM) layer is selected. For this study, we consider the meteorological inputs recorded no longer than seven days before the date the SAR image is captured, leading to two soil moisture layers. These two records will be referred to as L8 and L9, with L9 being the most recent record. The meteorological layers will be interpolated using ordinary kriging to match the spatial resolution of SAR images. Table 1 summarizes all of the datasets and pre-processes used in this study.

Table 1. Summary of geo-morphic, meteorological datasets, and SAR images used in this study

Item	Reference in this study	Spatial Resolution	Temporal Resolution	Pre-Processing	Data Availability
HAND	L1	10 m	-	Mosaic, Clip, Pixel align	NFIE Data Repository
Land Cover	L2	10 m	-	Mosaic, Clip, Pixel align	GEE
Precipitation	L3 to L7	0.1 degree	Every 30 min	Sum, Clip, Pixel align, Interpolation	GEE
Soil Moisture	L8 and L9	10,000 m	Every ~3 days	Clip, Interpolation, Pixel align	GEE
SAR Images	L10	10 m	Every 12 days for each satellite	Remove speckle noise	GEE

In addition to the listed pre-processing steps, all data layers with a different geo-projection will be converted into WGS84. After we stacked all the layers from the above sources together, we sliced those big multi-layer images into 256-by-256-pixel patches. Earth surface observations such as SAR images can be highly unbalanced in terms of the numbers of water body pixels and hillslope pixels (constantly dry pixels) (Zheng et al., 2020; Bai et al., 2021). To avoid wasting time and resources on predicting dry pixels on which there will be limited changes in backscatters regardless of weather conditions, we did a final filtering to remove patches without noticeable water bodies inside using the land cover feature. After all those processes and filtering, we obtained 11,601 eleven-layer 256-by-256-pixel image patches, among which one layer will be the target image and will not be used directly as input. We then split those patches into training, validation, and test sets with a 7:2:1 ratio.

3. Model Implementation

The forecasting framework in this study is created with a modified MA-Net with ResNet50 as the backbone. MA-Net is introduced by Fan *et al.*, (2020). It adopts the basic structure of U-Net introduced by Ronneberger *et al.*, (2015) but is implemented with a self-attention mechanism to integrate the local features of input with the global dependencies to achieve higher accuracy for liver and tumor segmentation. The model structure is shown in Figure 2.

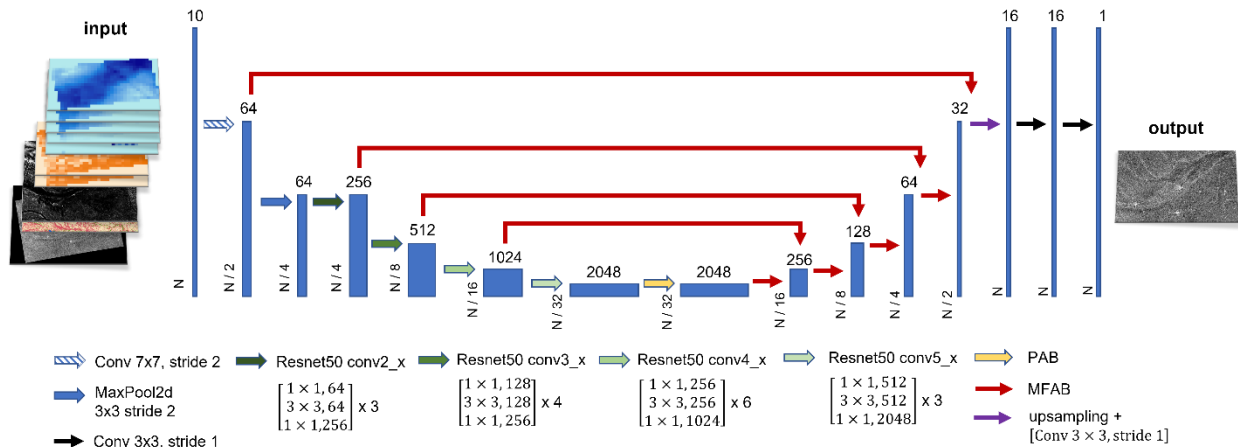


Figure 2. The model structure of the MA-SARNet proposed in this study

The Position-wise Attention Block (PAB) and Multi-Scale Fusion Attention Block (MFAB) depicted in Figure 2 have almost identical structures to the MFAB and PAB modules introduced in the original MA-Net paper by Fan *et al.*, (2020). We merely modified the channel numbers of the convolution layers of those two modules to fit our image dimension. Readers are encouraged to check the original MA-Net paper for details of the PAB and MFAB modules.

With respect to the selection of model structure, we compared a few state-of-the-art deep learning structures (i.e., DeepLab, EfficientNet, U-Net, and MA-Net), and backbones (i.e., MobileNet and ResNet) to help us decide on the most optimal model for this study. The combination of the MA-Net structure and the ResNet50 backbone provided us with the best performance at a reasonable running time and computational requirements. Since the focus of this study is not to compare different deep learning model structures, we will not elaborate on model selection in this paper.

The entire framework was implemented using PyTorch and trained on four Tesla K80 GPUs. We adopted an initial learning rate of $5E-4$, a batch size of 64 patches, and an Adam optimizer with the two beta parameters being 0.9 and 0.98, respectively. We also set a learning rate scheduler to gradually decrease the learning rate when the performance plateaued. As the loss function calculated with Eq. 1, we used a combination of mean absolute error (MAE) and (1 - Nash-Sutcliffe efficiency (NSE)).

$$Loss_{FN} = 0.5 \times MAE + 0.5 \times (1 - NSE) \quad (1)$$

4. Results and Discussion

4.1. Evaluation Indices and Benchmark Performance

As mentioned in the previous section, our model uses 10 input layers containing physical information to predict the VV band of backscatters for SAR images. Because the predictions and target values are numbers rather than categorical variables, it is unlikely that those values will exactly match every digit. Therefore, we adopted MAE, NSE, and Sinkhorn Divergences (SD) to measure the similarity between predictions and target values. MAE is a scale-dependent accuracy index that measures the average difference among prediction-target pairs. MAE varies between 0 and positive infinity, where 0 means no error/difference. MAE (Eq. 2) is calculated as:

$$MAE = \frac{\sum_{i=1}^n |pred_i - obs_i|}{n} \quad (2)$$

NSE indicates the predictive skill of a model by measuring the relative magnitude of the residual variance against the measured data variance (Nash and Sutcliffe 1970). The NSE ranges between -infinity and 1, where 1 means a perfect match, 0 means the quality of predictions is equal to simply taking the mean of the observations, and less than 0 means predictions are even worse than the mean value. NSE (Eq. 3) is calculated as below:

$$NSE = 1 - \frac{\sum_{i=1}^n (pred_i - obs_i)^2}{\sum_{i=1}^n (obs_i - \overline{obs})^2} \quad (3)$$

SD measures the geometric divergences between the predicted and target images, with a focus on the similarity between the predicted and target probability distributions. Similar to Wasserstein distance (Earth Mover's Distance), SD measures how difficult it is to convert one distribution to another but is more computationally efficient. SD is defined as:

$$SD(pred, obs) = OT - \frac{1}{2}OT(pred, pred) - \frac{1}{2}OT(obs, obs) \quad (4)$$

OT is the Optimal Transport problem with entropic regularization defined by Oneto et al., (2020). SD is a nonnegative value. The smaller the SD is, the more similar the predictions are to the observations. In this study, we adopted the implementation of the GeomLoss library to calculate SD. Because the above three evaluation indices are not on the same scale and focus on different aspects of model performance, we develop an assemble accuracy index (AAI) that takes them all into account to facilitate comparison. AAI is calculated as:

$$AAI = \frac{1}{1 + MAE} + \frac{1}{1 + SD} + NSE \quad (5)$$

Since MAE and SD are both nonnegative figures that vary among $[0, +\infty)$, the first two terms to the right-hand side of Eq. (5) will be projected to the range of $(0, 1]$, where 1 is the best possible matching scenario for both. Given that the higher the better also applies to the third component of the right-hand side of Eq. 4, a higher AAI will indicate a better match between predictions and observations. Note that the way we create AAI makes it sensitive to changes in NSE. Therefore, although NSE can vary over a larger range, it will be well reflected in AAI. For result visualization purposes, we will display both NSE and AAI, as the former is a major component of AAI. But it is good to keep in mind that when we compare results quantitatively, we will only consider AAI.

Due to the shortage of relevant studies, we constructed the benchmark performance with the temporal persistence assumption—current backscatter values equal the temporally nearest previous backscatter values. We compute all the above-mentioned evaluation indices by taking the previous backscatter values as predictions and will use those values as the benchmark performance to evaluate the model's performance and robustness. Persistence was proven to be a simple but powerful assumption in streamflow forecasting tasks (Krajewski et al., 2021) and has been adopted in some recent works in image synthesis tasks (Diaconu et al., 2022; Sit et al., 2022) to create benchmark performance as well.

4.2. Synthesized SAR-Image and Corresponding Flood Extent

Figure 3 shows the box plot of AAI and NSE on the test set predicted with the benchmark method and model. Each circle represents the AAI or NSE value of an image patch. The model performance is achieved by inputting a combination of HAND (L1), land cover (L2), all precipitation layers except for the last one (L3-L6), the soil moisture information collected between four and seven days ahead of the SAR capture date (L8), and the previous VV band of SAR (L10). This is the best combination we found out of all the possible input layer combinations we tested (also see the results in the following subsection). The mean and median values of NSE generated with the benchmark method with the persistence assumption fell into categories of "satisfactory" and "good," respectively, according to the performance rating for NSE introduced by Moriasi et al., (2007). Although that performance rating was concluded from time series analyses with a monthly time step, it still provides readers with a basic idea about the prediction power of the model and benchmark method, given the absence of the corresponding performance rating for this specific topic.

Figure 3 also shows that our model greatly improved prediction quality compared to the benchmark performance. More specifically, the mean values of AAI and NSE increased by 31.9% and 37.9%, respectively, and the median values of those two indexes increased by 17.8% and 15.1%. The improvement indicates that even though pixels on the previous and current satellite images shared a lot of similarities, taking into account meteorological and geomorphic inputs will still provide additional useful information that will further improve prediction quality. In addition to the increases in the mean and median values, the AAI and NSE data points showed that predictions considering meteorological and geomorphic factors were less spread out. In

other words, those additional data helped correct cases (image patches) where there are major pixel-level divergences in backscatter between the previous and the current scene and therefore reduced the performance variation among different cases.

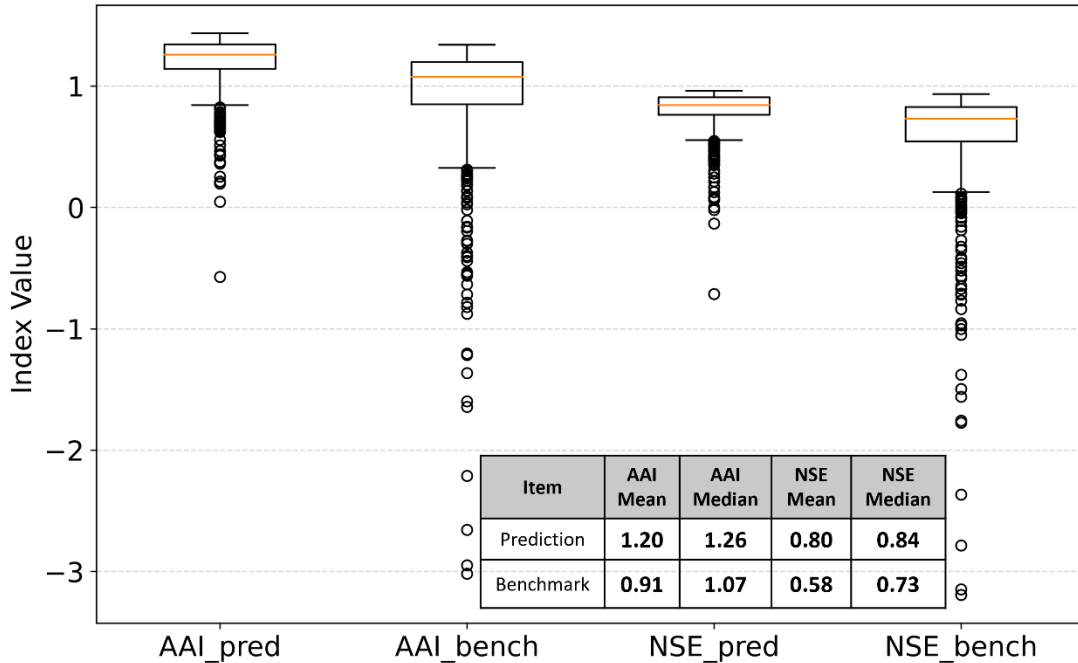


Figure 3. The box plot of AAI and NSE of predictions and the benchmark on the test set

Figure 4 shows the real SAR image backscatter of the VV band (VV_Label), the corresponding predictions by the model (VV_Pred) on the test set, the flood extent derived from VV_Label using Otsu’s thresholding method (Extent_Label), the flood extent derived from the predicted VV backscatters (Extent_Pred) using the same thresholding method, and two additional flood extent maps. The Extent_NASA column was generated by NASA’s Marshall Space Flight Center (MSFC), and the Extent_FAC maps were created by Yang et al., (2021) as an open access SAR-based flood extent archive.

Comparing the target images and the predictions, the model successfully predicted all structural characteristics shown on the label image, even in cases where structures are quite complex, such as scenes #3 and #5. In addition, pixel groups with significant backscatter divergence from adjacent pixels, such as the bottom bright part on scene #4, are well preserved in predictions. The visual comparison between the flood extent extracted from the target and the predicted image and the comparison between the extracted flood extent and those from the other two data sources also confirmed the efficacy of our model, as the structure and overall shape of Extent_Pred are comparable to those of the other three flood extent columns. We also noticed that, compared to the target image, the prediction, in general, looks a little blurry, especially in dry areas (light gray areas) in scenes #1, #2, and #4, and is less noisy. This means each pixel on the prediction has a smaller difference in values from its neighboring pixels, whereas the value

difference between neighboring pixels is more significant on the target image. We believe this is attributable to two main factors: first, the meteorological data layers are downscaled products from a very coarse original resolution. Therefore, even though the kriging interpolation increased their spatial resolution to match that of the SAR pixels, they are still less rich in terms of the details carried by each pixel and thus make the prediction less detailed compared to the target image. Secondly, the convolution and pooling processes, especially when they involve changes in the size of image patches, may also remove some of the details from the input layers and therefore create a slight blurring effect on the prediction.

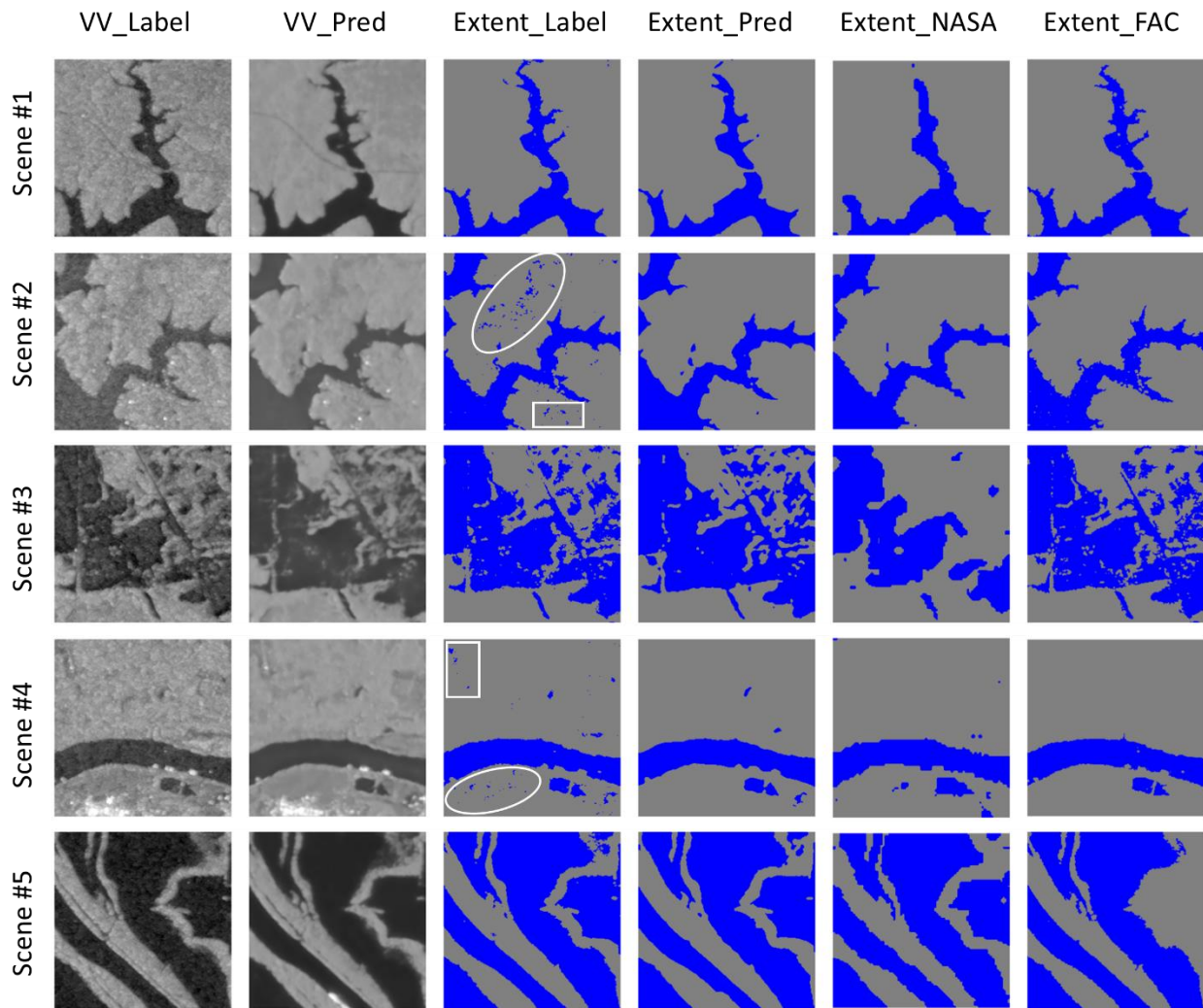


Figure 4. The target and prediction of the VV band of SAR images (first two columns), corresponding flood extents derived using the Otsu thresholding method (two columns in the middle), and two flood extent map archives created by other researchers (last two columns)

In most geospatial analyses and water resources applications, such as land-use-land-cover classifications and flood extent extractions, we care more about pixel clusters and how those clusters are different from each other than focusing on the characteristics of single pixels.

Moreover, we tend to treat isolated pixels that behave differently compared to their neighbors as abnormal pixels or noise and often want to correct the classes (i.e., flood or dry) of those isolated pixels using the neighboring dominant class (Liang and Liu 2020; Zhang et al., 2020). With that in mind, we believe the moderate blurring effect of the model is favorable. As shown in Figure 4, the predicted flood extent (Extent_Pred) avoided some noisy mispredictions generated with the target image, such as those isolated flood pixels inside white boxes in scenes #2 and #4. Furthermore, removing speckle noise is a necessary preprocessing step when dealing with SAR images, with the goal of also adjusting the pixel values using adjacent values to reduce the difference between neighboring pixels. The speckle noise removal step will also create a blurry effect on images, which is very inevitable and widely accepted. Given the above reasoning, we believe the slightly blurry effect in predicted images is not very concerning.

4.3. Model Performance with Different Input Combinations

Table 2 shows the model's performance with different combinations of input layers. L1 and L2 are the HAND, and the land cover map, respectively. L3–7 are the five layers of accumulative precipitation (0–24 hours, 25–48 hours, 49–72 hours, 73–120 hours, and 121–168 hours prior to the SAR capture timestamp). L8 and 9 are the two soil moisture products collected no longer than seven days prior to the date for which we predict the SAR image. L10 is the previous SAR image of the same position that is closest in time. We just showed a part rather than the entire configuration collection we tested to reduce information redundancy.

Table 2. Model performance with different combinations of input layers (displaying examples from all configurations tested). The best input combination and results are marked in gray.

Item	MAE	MAE	SD	SD	NSE	NSE	AAI	AAI
	Mean	Median	Mean	Median	Mean	Median	Mean	Median
L12345678910	1.57	1.43	622.38	436.22	0.79	0.85	1.19	1.26
L1234567910	1.67	1.49	1046.88	479.60	0.59	0.83	0.98	1.23
L1234567810	1.59	1.43	627.93	443.49	0.79	0.84	1.19	1.25
L123456810	1.58	1.43	615.32	432.40	0.80	0.84	1.20	1.26
L1234568	2.01	1.79	975.27	693.02	0.67	0.75	1.02	1.10
L10	1.74	1.55	764.09	521.08	0.74	0.73	1.12	1.22
Benchmark	2.20	1.93	1164.58	833.26	0.58	0.73	0.91	1.07

Here, we adopted the idea of reduced error pruning (Esposito et al., 1999), which is similar to the backward selection introduced by Halinski and Feldt (1970). We started with all ten variables (layers), trained the model, and checked its performance on the test set. If removing a layer does not significantly reduce the predicting power of the model, then the layer will be removed. We repeated this process until no more layers could be removed. The optimal combination of inputs (L123456810) is shown in Table 2, shaded with light gray.

Comparing the first three rows in Table 2, it is obvious that the soil moisture information that is temporally closer to the SAR capture date, namely L9, brings less improvement compared to the further one, namely L8. When L8 is removed, a noticeable drop in model performance occurs. By contrast, removing L9 only leads to nuance. Similar to the case of L9, we noticed that removing the layer of the accumulative precipitation (L7) over 121–168 hours prior to the SAR capture timestamp only leads to a trivial difference. Those results indicate that among all the precipitation involved, the temporally closer precipitation is more influential compared to the further away one. On the contrary, for soil moisture information, the temporally further away one has a stronger impact compared to the closer one. The efficacy of the combination of closer precipitation and further away soil moisture may also be the reason that L7 and L9 are unnecessary, as the contributing information of L7 may already be contained in the further away soil moisture layer, and the closer precipitation information also describes the closer soil condition well enough.

The comparison between the last four rows confirmed the forecasting power of the model if it is trained with appropriate inputs. We noticed that if we remove the layer of the previous SAR from the input, the performance will drop significantly. This is because although meteorological and geomorphic factors are driving forces for the backscatter values of SAR images, backscatter values are mostly determined by surface characteristics, such as surface roughness, that are independent of or less likely to be influenced by those factors. In other words, the base tone of the backscatter value can be considered independent of meteorological and geomorphic factors and is carried only in the previous SAR image layer among all input layers considered in this study. Although the land cover layer is a strong representative of the surface characteristics, it indicates more about the clustering of adjacent pixels than every single pixel. In addition, the classifications of the land cover layer are human interpretations involving other social factors that may not be consistent with real natural phenomena, such as distinguishing between grassland and crop fields. The same applies to HAND map data. Although HAND mapping is a strong indicator of water and non-water clusters, its value, especially for hillslope pixels, is determined more by the distance between a pixel and the drainage channel than the surface characteristics. Similarly, training with only the previous backscatters will not bring a better result than in the case where geomorphic, meteorologic, and previous backscatters all come into play.

4.4. Robustness Tests

Figure 5 demonstrates the model's generalization power on scenes that it has not seen before in the training-validation-test division. Table 3 lists the corresponding quantitative summary. Notice that, in this section, the discussion will be all about the performance of the best model configuration (L123456810) found in the previous section.

As shown in Figure 5 and Table 3, the model achieved better performance as measured by all four evaluation indices in all four scenes compared to the benchmark performance. The average improvement in the mean and median AAI for the two temporal test scenes is 9.0% and 7.2% (52

FC) and is 8.0% and 6.3% (8814). For the two temporal cases, the mean and median AAI are 14.1% and 12.6% (086E) and 9.0% and 7.2% (1544) for the two spatial test scenes. The performance enhancement of AAI for all four robustness scenarios is lower compared to the increase on the test set, where an increase of 31.9% (mean AAI) and 17.8% (median AAI) is achieved. This indicates that the model has successfully learned the mathematical relationship between input-output pairs during the training stage but did not overfit it. If the opposite happens, where the model performs better on scenes it has never seen before (either temporally or spatially) than on scenes with patterns it should already be familiar with from the training stage, then chances are there is something wrong with the model setup or training process.

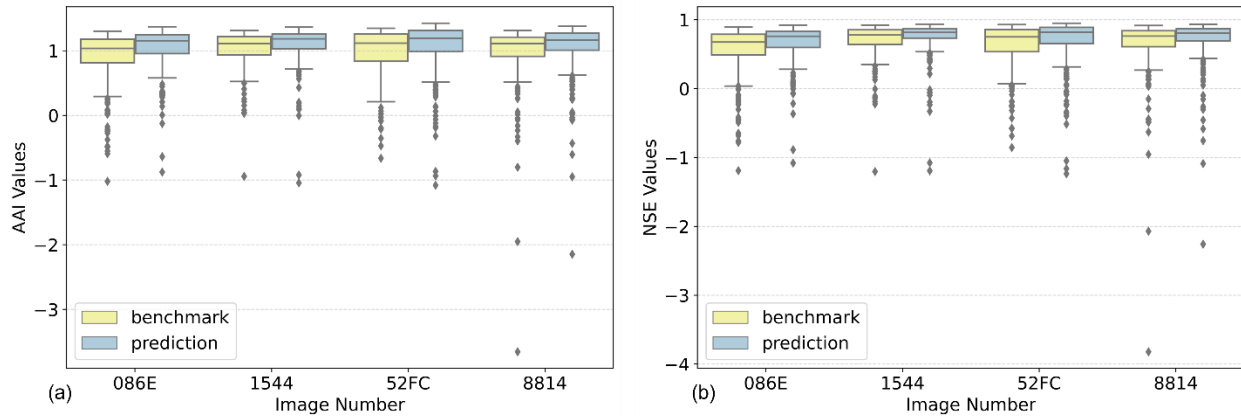


Figure 5. Box plots of model performance in terms of NSE and AAI in the four robustness test scenes

Table 3. Summary of the model's generalization power in the four scenes from robustness test

Image No.	Item	MAE	MAE	SD	SD	NSE	NSE	AAI	AAI
		Mean	Median	Mean	Median	Mean	Median	Mean	Median
086E	Prediction	1.76	1.55	686.13	531.03	0.67	0.76	1.05	1.16
	Benchmark	1.92	1.78	869.54	674.30	0.57	0.68	0.92	1.03
1544	Prediction	2.06	1.85	1014.10	761.40	0.75	0.82	1.09	1.18
	Benchmark	2.19	2.05	1125.58	892.17	0.67	0.77	1.00	1.10
52FC	Prediction	1.80	1.63	788.76	584.40	0.73	0.82	1.10	1.19
	Benchmark	2.02	1.78	966.33	658.70	0.66	0.75	1.01	1.11
8814	Prediction	1.95	1.80	926.33	697.20	0.73	0.80	1.08	1.16
	Benchmark	2.13	1.92	1088.26	814.18	0.67	0.76	1.00	1.11

Similar to what we saw in Figure 4, the flood extent derived from the predicted image avoided mismatches caused by noisy pixels, which occurred not only as false positive predictions (flooded pixels in locations where no flood was observed), such as those inside the white box on scene #4, but also as false negative predictions (dry pixels in locations where flood occurred), such as those inside the white box on scene #1. Normally, qualitative and quantitative factors,

including connectivity, should be taken into consideration when deciding whether a pixel is a false positive or false negative. Here, we are just judging them with a combination of visual connectivity, common sense (for instance, it is unlikely that there are that many isolated dry pixels in a real river segment as shown in the last figure in scene #1), and by comparing them with maps from the other sources. We saw that there were also some imperfections on the maps generated by NASA (i.e., the Extent_NASA of scene #3 in Figure 4 and the Extent_NASA of scene #2 in Figure 5) and on those provided by FAC (i.e., the Extent_FAC of scene #1 in Figure 5). Given that those flood maps in the last two columns are already the most trustworthy SAR-based flood map sources the authors can find, as they either come from the US federal research institution or have been evaluated against flood maps generated by other federal institutions (i.e., USGS) and have reported substantial agreements (Yang et al., 2021), the discrepancy between these two map sources in some scenes demonstrated the difficulty of flood extraction based on SAR and therefore further demonstrated the accuracy and predicting power of our model.

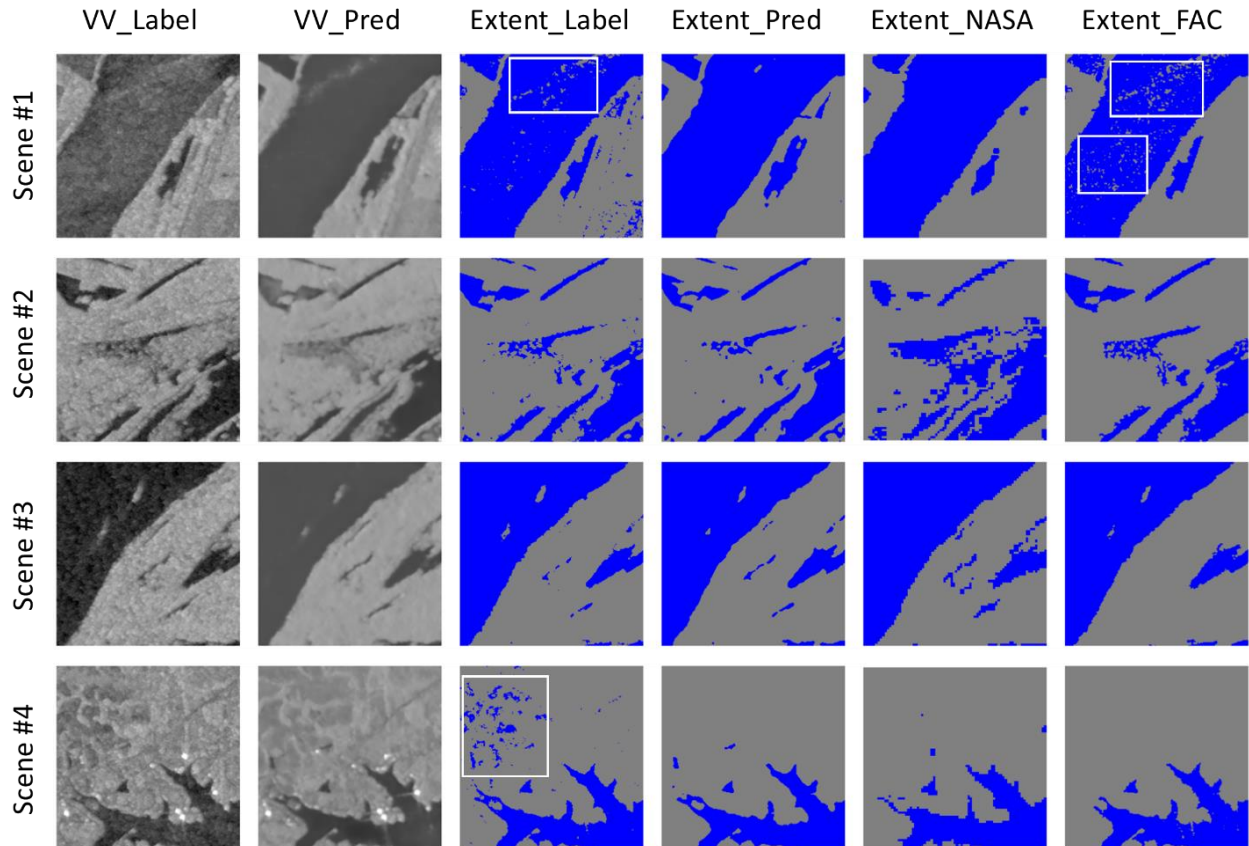


Figure 6. Examples of the target and prediction of the VV band of SAR from robustness testing cases, corresponding flood extents derived using the Otsu thresholding method, and the two columns of flood extent maps from NASA's MSFC and FAC

5. Uncertainty and Parameter Sensitivity Analysis

5.1. Input Downscaling Using Spatial Interpolation

The uncertainty of this study mainly comes from the downscaling process used to match the coarse meteorological data layers to the high-resolution SAR images. Currently, the most widely studied downscaling techniques are statistical and dynamical. Dynamical downscaling approaches require regional climate models (RCMs) or weather models to compute high-resolution meteorological layers by simulating physical processes (Sharifi et al., 2019). Whereas statistical approaches derive high-resolution data layers using the relationship between the dependent datasets and auxiliary data layers such as vegetation and topography indexes (López López et al., 2018). Although those two approaches may be more accurate compared to other methods, they require huge computational resources and data dependencies, which often makes them impractical for data-driven applications such as those using deep learning models, especially those that need to downscale daily data, such as our study.

More specifically, in our study, each eleven-layer image stack includes seven meteorological data layers (five precipitation and two soil moisture layers), which leads to a requirement of at least 238 (34 images in total) 10-m resolution auxiliary datasets assuming the usage of one auxiliary layer for each coarse meteorological layer we try to downscale to build the regression relationship with. If the auxiliary data are coarser than the SAR images, extra interpolation will still be needed. In most cases, more than one auxiliary data layer is needed for downscaling one coarse meteorological input, and those auxiliary data themselves can be secondary products that need to be derived from other datasets. Given that, although it could be less accurate to simply derive the finer-resolution data layer using geo-interpolation, it keeps a better balance between the computational cost and performance for large-scale applications using deep learning models such as ours. Another widely used input downscaling approach for applications with deep learning models is resampling (Sharifi et al., 2019; Requena-Mesa et al., 2021; Dasgupta et al., 2022).

5.2. Inconsistent between Input Layers

Another uncertainty source is the data inconsistency between geomorphic input layers. Although each data layer involved in this study comes from trustworthy institutions and agencies and is widely documented in the literature (Friedl et al., 2022; Wang, Yang, et al., 2022; Garousi-Nejad, 2022), it is still inevitable that there can be minor inconsistencies between those layers as they are created independently following separate data processing protocols with different software and data dependencies collected in different conditions and times. We manually checked the data consistency before feeding it into the forecasting workflow to ensure that different data layers are spatially consistent, but we did find some cases where there are discrepancies between those layers. Figure 7 shows the HAND and the land cover map for the same location.

As shown in Figure 7 in the red circle, there are some mismatches between HAND and the land cover map. For the open water area on the land cover map, the water surface must be

present for the majority of the year in order to be classified as open water rather than any other class. By contrast, the HAND values for the bright pixels inside the red circle vary between 4 and 10 meters, meaning those pixels are at least 4 meters above the stream pixels (river channel pixels) and therefore are not considered channel pixels, meaning they are less likely to be under water for a long time, according to the HAND map. Fortunately, these inconsistencies just occurred in a very small number of samples.

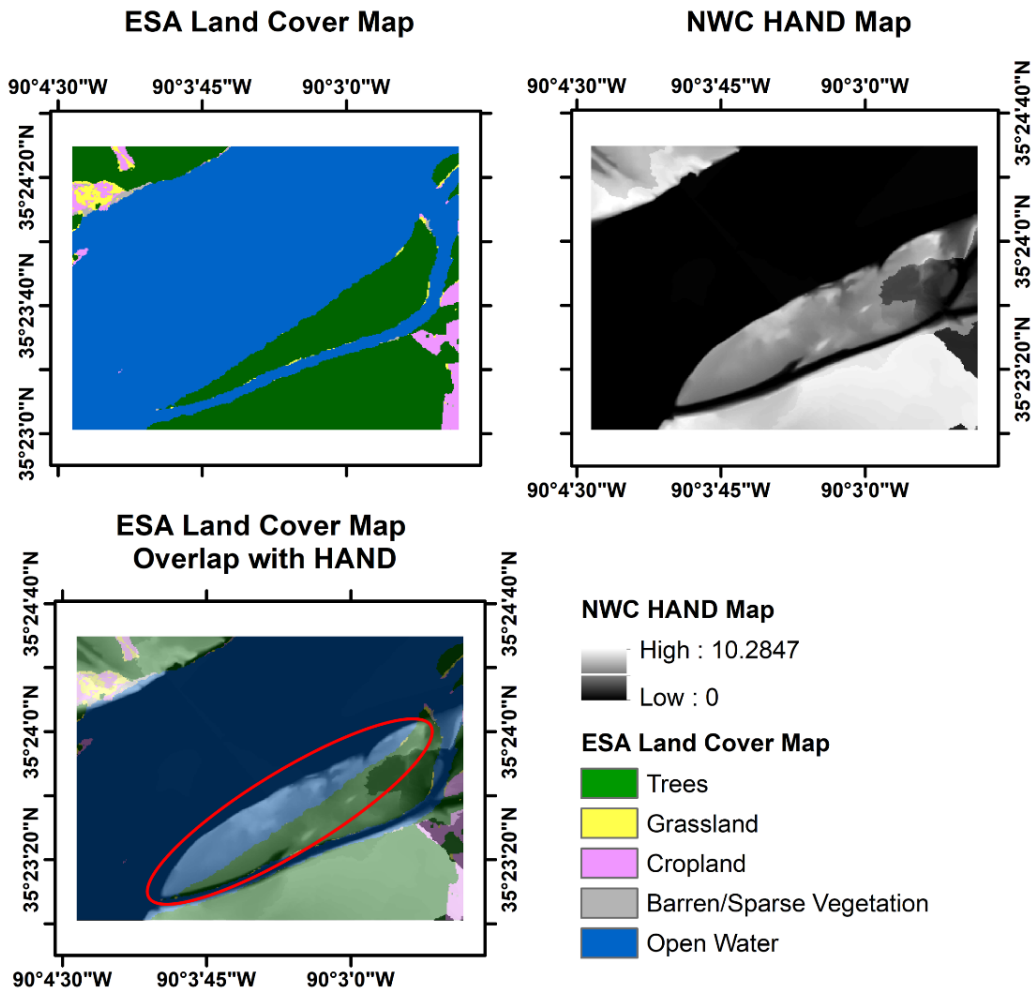


Figure 7. A case where the geomorphic layers show noticeable inconsistency

While it seems like a reasonable practice to pick one as a reference and force the other to align with it, it brings two additional issues. First, using either the land cover or the HAND as a reference will introduce selection bias into the results. Moreover, pixels on the land cover map are categorical, while they are numerical on the HAND map. Therefore, it will add extra uncertainty to the results if we try to speculate on HAND values based on their land cover classifications or try to categorize pixels into different land cover classes based on their HAND values. Given the preceding reasoning, as well as the limited number of pixels of disagreement, neither the land cover map nor the HAND map were modified.

5.3. Variation in Model Performance Due to Artificial Changes in Precipitation and Soil Moisture Layers

Table 4 shows model performance with an artificial increase or decrease of 10% for the four precipitation and one soil moisture layer of the best input combination of L123456810. We first noticed that the median of NSE is quite stable throughout all configurations. Besides that, the only case that brought a tiny performance increase for some other evaluating matrices is the one with L4 decreasing by 10%, whereas all the other variations led to either almost equal or slightly worse performance. Comparing the two variations for the same input layers ($\pm 10\%$ cases for the same layer), we see that the performance is more sensitive to input increases than decreases. Moreover, each evaluating index reacts differently to the same change. For instance, the median value of NSE does not change as much as the mean of NSE does. The same applies to SD. Whereas MAE is more complicated, the mean value sometimes gets more volatile than the median, while the opposite also happens in other cases. Last but not least, increasing L6 by 10% brings the most significant changes in model performance compared to all the other cases, followed by increasing L4 by 10%.

Table 4. Model performance with 10% variation of precipitation input. The one without input variations is shaded in light gray.

Item	MAE	MAE	SD	SD	NSE	NSE	AAI	AAI
	mean	median	mean	median	mean	median	mean	median
L123456810	1.58	1.43	615.32	432.40	0.80	0.84	1.20	1.26
L3+10%	1.59	1.45	632.75	445.54	0.79	0.84	1.19	1.26
L3-10%	1.59	1.43	630.40	439.88	0.79	0.85	1.19	1.26
L4+10%	1.59	1.45	762.58	455.58	0.74	0.85	1.14	1.25
L4-10%	1.56	1.42	614.24	431.35	0.79	0.84	1.20	1.26
L5+10%	1.60	1.46	664.02	460.18	0.77	0.84	1.17	1.25
L5-10%	1.60	1.43	646.86	445.11	0.78	0.85	1.18	1.26
L6+10%	1.64	1.48	1,095.11	471.23	0.65	0.84	1.04	1.24
L6-10%	1.58	1.44	717.67	448.10	0.76	0.84	1.16	1.26
L8+10%	1.59	1.43	755.87	443.70	0.75	0.84	1.15	1.25
L8-10%	1.58	1.43	620.57	435.10	0.79	0.84	1.19	1.25

6. Conclusion

In this study, we proposed MA-SARNet, a one-shot SAR image forecasting framework built with a modified MA-Net, to predict pixel-level backscatter values of SAR images in response to meteorological and geomorphic driving forces. The model performance was evaluated against the benchmark performance created with the temporal persistence assumption and was compared against the label image, label water extent, and two independently validated flood maps.

Visual comparisons showed that the predicted backscatter values not only got all structural characteristics and shapes correct but also maintained pixel groups that showed significant

backscatter divergence from adjacent pixels. The model demonstrated stable performance even with cases containing complex structures and shapes. In addition, there were fewer noise pixels on the predicted image compared to the label image, which can, therefore, improve the robustness of the derived flood extent against mismatches caused by pixel-level noise. More specifically, it helps reduce the number of misclassified dry pixels (false negatives) as well as incorrect water pixels (false positives) compared to the extent derived from the target image and the other two flood extent map references.

Results suggested that the best combination of input layers consists of HAND, land cover, accumulative precipitation layers summed over 0–24 hours, 25–48 hours, 49–72 hours, and 73–120 hours prior to the timestamp, the soil moisture conditions within four to seven days before the SAR capture date, and the most recent previous SAR layer. The result also indicates that SAR contains surface characteristic details that are not included in geomorphic and meteorological layers, and vice versa. Therefore, removing the previous SAR image will cause a noticeable drop in model performance. Similarly, using only the previous SAR image for training will lead to worse performance. The model's spatial and temporal generalization power was tested using four images saved separately from the training, validation, and test sets, and the model showed satisfying generalization power compared to the benchmark in both the spatial and temporal testing cases.

The uncertainty of the predictions mainly comes from the downscaling process to match the resolution of the meteorological input layers with the high-resolution SAR image bands and other geomorphic layers. Another source of uncertainty is the inconsistency between data layers. Currently, the model does not consider inputs related to snow cover or snow melt conditions and thus may not perform well when snow melt dominates the flooding process. Sensitivity analysis showed that, given $\pm 10\%$ variations in the meteorological factors involved in this study, model performance is more sensitive to an increase in input than a decrease. Overall, the model performed slightly worse with input variations, regardless of whether they were increasing or decreasing. The results also indicated that variations in certain input layers, such as L4 and L6, are more influential on model performance compared to other layers. However, further investigation is needed to understand the underlying reason and whether it applies to other regions.

Overall, the proposed one-shot forecasting model is not constrained to SAR backscatter predictions but is applicable to other remotely sensed imagery, such as optical images (i.e., Landsat products and Sentinel-2 images). This model only requires a few publicly accessible meteorological and geomorphic layers and the previous SAR as input, which therefore makes the forecasting framework easily applicable to other regions around the world. The generalization power shown by the robustness test demonstrates the potential of this model for usage scenarios including large-scale real-time earth surface predictions that will aid in fast response and mitigation tasks against future floods.

7. Acknowledgement

We would like to acknowledge Lori A. Schultz and her colleagues at NASA's Marshall Space Flight Center for providing flood inundation extent maps (the Extent_NASA column in Figures 4 and 6) for comparison in this study.

8. Reference

- Alabbad, Y., Mount, J., Campbell, A.M., and Demir, I., 2021. Assessment of transportation system disruption and accessibility to critical amenities during flooding: Iowa case study. *Science of the Total Environment*, 793.
- Alabbad, Y., Yildirim, E., and Demir, I., 2022. Flood mitigation data analytics and decision support framework: Iowa Middle Cedar Watershed case study. *Science of the Total Environment*, 814, 152768.
- Amini, A., Dolatshahi, M., and Kerachian, R., 2022. Adaptive precipitation nowcasting using deep learning and ensemble modeling. *Journal of Hydrology*, 612, 128197.
- Aristizabal, F., Judge, J., and Monsivais-Huertero, A., 2020. High-resolution inundation mapping for heterogeneous land covers with synthetic aperture radar and terrain data. *Remote Sensing*, 12 (6), 900.
- Atefi, M.R. and Miura, H., 2022. Detection of Flash Flood Inundated Areas Using Relative Difference in NDVI from Sentinel-2 Images: A Case Study of the August 2020 Event in Charikar, Afghanistan. *Remote Sensing*, 14 (15), 3647.
- Bai, Y., Wu, W., Yang, Z., Yu, J., Zhao, B., Liu, X., Yang, H., Mas, E., and Koshimura, S., 2021. Enhancement of detecting permanent water and temporary water in flood disasters by fusing sentinel-1 and sentinel-2 imagery using deep learning algorithms: Demonstration of sen1floods11 benchmark datasets. *Remote Sensing*, 13 (11), NA.
- Bosch, M., Conroy, C., Ortiz, B., and Bogden, P., 2020. Improving emergency response during hurricane season using computer vision. In: *Earth Resources and Environmental Remote Sensing/GIS Applications XI*. SPIE, 14.
- Chaudhuri, C., Gray, A., and Robertson, C., 2021. InundatEd-v1.0: a height above nearest drainage (HAND)-based flood risk modeling system using a discrete global grid system. *Geosci. Model Dev*, 14, 3295–3315.
- Cherif, I., Ovakoglou, G., Alexandridis, T.K., Kganyago, M., and Mashiyi, N., 2021. Improving water bodies detection from Sentinel-1 in South Africa using drainage and terrain data. In: <https://doi.org/10.1117/12.2599671>. SPIE, 35.
- Choi, W. IL, Kim, E.S., Yun, S.J., Lim, J.H., and Kim, Y.E., 2021. Quantification of one-year gypsy moth defoliation extent in wonju, korea, using landsat satellite images. *Forests*, 12 (5), 545.
- Chowdhury, T., Murphy, R., and Rahnemoonfar, M., 2022. RescueNet: A High Resolution UAV Semantic Segmentation Benchmark Dataset for Natural Disaster Damage Assessment.
- Dasgupta, A., Hybbeneth, L., and Waske, B., 2022. Towards Daily High-resolution Inundation Observations using Deep Learning and EO.
- Demiray, B.Z., Sit, M., and Demir, I., 2021a. DEM Super-Resolution with EfficientNetV2. arXiv preprint arXiv:2109.09661.
- Demiray, B.Z., Sit, M., and Demir, I., 2021b. D-SRGAN: DEM Super-Resolution with Generative Adversarial Networks. *SN Computer Science*, 2 (1), 1–11.
- Diaconu, C.-A., Saha, S., Gunnemann, S., and Xiang Zhu, X., 2022. Understanding the Role of Weather Data for Earth Surface Forecasting using a ConvLSTM-based Model. 1361–1370.

- Dong, Z., Wang, G., Amankwah, S.O.Y., Wei, X., Hu, Y., and Feng, A., 2021. Monitoring the summer flooding in the Poyang Lake area of China in 2020 based on Sentinel-1 data and multiple convolutional neural networks. *International Journal of Applied Earth Observation and Geoinformation*, 102, 102400.
- ESA, 2013. User Guides - Sentinel-1 SAR - Sentinel Online - Sentinel Online [online]. *Sentinels.copernicus.eu*. Available from: <https://sentinel.esa.int/web/sentinel/user-guides/sentinel-1-sar> [Accessed 30 Sep 2022].
- Esfandiari, M., Jabari, S., McGrath, H., and Coleman, D., 2020. Flood mapping using random forest and identifying the essential conditioning factors; A case study in fredericton, new brunswick, Canada. In: *ISPRS Annals of the Photogrammetry, Remote Sensing and Spatial Information Sciences*. 609–615.
- Esposito, F., Malerba, D., Semeraro, G., and Tamma, V., 1999. Effects of pruning methods on the predictive accuracy of induced decision trees. *Applied Stochastic Models in Business and Industry*, 15 (4), 277–299.
- Ewing, G. and Demir, I., 2021. An ethical decision-making framework with serious gaming: A smart water case study on flooding. *Journal of Hydroinformatics*, 23 (3), 466–482.
- Fan, T., Wang, G., Li, Y., and Wang, H., 2020. Ma-net: A multi-scale attention network for liver and tumor segmentation. *IEEE Access*, 8, 179656–179665.
- Flanagan, P.X., Mahmood, R., Umphlett, N.A., Haacker, E., Ray, C., Sorensen, W., Shulski, M., Stiles, C.J., Pearson, D., and Fajman, P., 2020. A Hydrometeorological Assessment of the Historic 2019 Flood of Nebraska, Iowa, and South Dakota. *Bulletin of the American Meteorological Society*, 101 (6), E817–E829.
- Friedl, M.A., Woodcock, C.E., Olofsson, P., Zhu, Z., Loveland, T., Stanimirova, R., Arevalo, P., Bullock, E., Hu, K.-T., Zhang, Y., Turlej, K., Tarrío, K., McAvoy, K., Gorelick, N., Wang, J.A., Barber, C.P., and Souza, C., 2022. Medium Spatial Resolution Mapping of Global Land Cover and Land Cover Change Across Multiple Decades From Landsat. *Frontiers in Remote Sensing*, 3.
- Garousi-nejad, I., 2022. Improving Flood Inundation and Streamflow Forecasts in Snowmelt Dominated Regions by. Utah State University.
- Gautam, A., Sit, M., and Demir, I., 2022. Realistic River Image Synthesis Using Deep Generative Adversarial Networks. *Frontiers in Water*, 4.
- Halinski, R.S. and Feldt, L.S., 1970. The Selection of Variables in Multiple Regression Analysis. *Journal of Educational Measurement*, 7 (3), 151–157.
- Haltas, I., Yildirim, E., Oztas, F. and Demir, I., 2021. A comprehensive flood event specification and inventory: 1930–2020 Turkey case study. *International Journal of Disaster Risk Reduction*, 56, p.102086.
- Hammond, M.J., Chen, A.S., Djordjević, S., Butler, D., and Mark, O., 2015. Urban flood impact assessment: A state-of-the-art review. *Urban Water Journal*, 12 (1), 14–29.
- Hayhoe, K., Wuebbles, D.J., Easterling, D.R., Fahey, D.W., Doherty, S., Kossin, J.P., Sweet, W. V., Vose, R.S., and Wehner, M.F., 2018. *Our Changing Climate. In Impacts, Risks, and Adaptation in the United States: Fourth National Climate Assessment, Volume II*. U.S. Global Change Research Program.
- He, K., Yang, Q., Shen, X., and Anagnostou, E.N., 2021. Western Europe flood in 2021: mapping agriculture flood exposure from SAR. *Natural Hazards and Earth System Sciences*, 22 (November), 1–8.
- Hu, A. and Demir, I., 2021. Real-time flood mapping on client-side web systems using hand

- model. *Hydrology*, 8(2), p.65.
- Huang, C., Nguyen, B.D., Zhang, S., Cao, S., and Wagner, W., 2017. A comparison of terrain indices toward their ability in assisting surface water mapping from sentinel-1 data. *ISPRS International Journal of Geo-Information*, 6 (5), 140.
- Kladny, K.-R., Milanta, M., Mraz, O., Hufkens, K., and Stocker, B.D., 2022. Deep learning for satellite image forecasting of vegetation greenness. *bioRxiv*, 2022.08.16.504173.
- Ko, J., Lee, K., Hwang, H., Oh, S.G., Son, S.W., and Shin, K., 2022. Effective training strategies for deep-learning-based precipitation nowcasting and estimation. *Computers and Geosciences*, 161, 105072.
- Krajewski, W.F., Ghimire, G.R., Demir, I., and Mantilla, R., 2021. Real-time streamflow forecasting: AI vs. Hydrologic insights. *Journal of Hydrology X*, 13, 100110.
- Li, Z., Mount, J., and Demir, I., 2022. Accounting for uncertainty in real-time flood inundation mapping using HAND model: Iowa case study. *Natural Hazards*, 1–28.
- Li, Z. and Demir, I., 2022a. A comprehensive web-based system for flood inundation map generation and comparative analysis based on height above nearest drainage. *Science of The Total Environment*, 828, p.154420.
- Li, Z. and Demir, I., 2022b. U-Net-based Semantic Classification for Flood Extent Extraction using SAR Imagery and GEE Platform: A Case Study for 2019 Central US Flooding. *EarthArxiv*, 3588. <https://doi.org/10.31223/X5V07T>
- Li, Z., Duque, F.Q., Grout, T., Bates, B. and Demir, I., 2023. Comparative analysis of performance and mechanisms of flood inundation map generation using Height Above Nearest Drainage. *Environmental Modelling & Software*, 159, p.105565.
- Liang, J. and Liu, D., 2020. A local thresholding approach to flood water delineation using Sentinel-1 SAR imagery. *ISPRS Journal of Photogrammetry and Remote Sensing*, 159, 53–62.
- Liu, Q., Huang, C., Shi, Z., and Zhang, S., 2020. Probabilistic river water mapping from Landsat-8 using the support vector machine method. *Remote Sensing*, 12 (9), 1374.
- Liu, Y.Y., Maidment, D.R., Tarboton, D.G., Zheng, X., Yildirim, A., Sazib, N.S., and Wang, S., 2016. A CyberGIS Approach to Generating High-resolution Height Above Nearest Drainage (HAND) Raster for National Flood Mapping. *The Third International Conference on CyberGIS and Geospatial Data Science*, (August), 1–5.
- López López, P., Immerzeel, W.W., Rodríguez Sandoval, E.A., Sterk, G., and Schellekens, J., 2018. Spatial downscaling of satellite-based precipitation and its impact on discharge simulations in the magdalena river basin in Colombia. *Frontiers in Earth Science*, 6, 68.
- Manavalan, R., Rao, Y.S., and Krishna Mohan, B., 2017. Comparative flood area analysis of C-band VH, VV, and L-band HH polarizations SAR data. *International Journal of Remote Sensing*, 38 (16), 4645–4654.
- Markert, K.N., Markert, A.M., Mayer, T., Nauman, C., Haag, A., Poortinga, A., Bhandari, B., Thwal, N.S., Kunlamai, T., Chishtie, F., Kwant, M., Phongsapan, K., Clinton, N., Towashiraporn, P., and Saah, D., 2020. Comparing Sentinel-1 surface water mapping algorithms and radiometric terrain correction processing in southeast Asia utilizing Google Earth Engine. *Remote Sensing*, 12 (15), 2469.
- Moharrami, M., Javanbakht, M., and Attarchi, S., 2021. Automatic flood detection using sentinel-1 images on the google earth engine. *Environmental Monitoring and Assessment*, 193 (5), 1–17.
- Moothedan, A.J., Thakur, P.K., Garg, V., Dhote, P.R., Aggarwal, S.P., and Mohapatra, M., 2020.

Automatic Flood Mapping Using Sentinel-1 Grd Sar Images And Google Earth Engine: A Case Study Of Darbhanga, Bihar, 'RS-GIS Applications in HydroMeteorological Disaster Management-One Day online Workshop' 15 May, 2018 View project PSInSAR Study of Lyngenfj.

- Moriassi, D.N., Arnold, J.G., Van Liew, M.W., Bingner, R.L., Harmel, R.D., and Veith, T.L., 2007. Model evaluation guidelines for systematic quantification of accuracy in watershed simulations. *Transactions of the ASABE*, 50 (3), 885–900.
- NASA, 2022a. Central US Flooding and Storms Spring 2019 | NASA Applied Science [online]. Available from: <https://appliedsciences.nasa.gov/what-we-do/disasters/disasters-activations/central-us-flooding-and-storms-spring-2019> [Accessed 23 Mar 2022].
- NASA, 2022b. Water Extent Map Produced Using Copernicus Sentinel-1 for Central US Flooding Late Spring 2019 in Vector Format - Overview [online]. Available from: <https://maps.disasters.nasa.gov/arcgis/home/item.html?id=28718006add84922b8531a2fadfbf2d3> [Accessed 30 Sep 2022].
- NASA, 2022c. Water Extent Map Produced Using Copernicus Sentinel-1 for Midwest Flooding March 2019 - Overview [online]. Available from: <https://maps.disasters.nasa.gov/arcgis/home/item.html?id=5027e1e1b7d141d19a910f303ed68685> [Accessed 30 Sep 2022].
- Nash, J.E. and Sutcliffe, J. V., 1970. River flow forecasting through conceptual models part I — A discussion of principles. *Journal of Hydrology*, 10 (3), 282–290.
- Oneto, L., Donini, M., Luise, G., Ciliberto, C., Maurer, A., and Pontil, M., 2020. Exploiting MMD and Sinkhorn Divergences for Fair and Transferable Representation Learning. *Advances in Neural Information Processing Systems*, 33, 15360–15370.
- Requena-Mesa, C., Benson, V., Reichstein, M., Runge, J., and Denzler, J., 2021. EarthNet2021: A large-scale dataset and challenge for earth surface forecasting as a guided video prediction task. *In: IEEE Computer Society Conference on Computer Vision and Pattern Recognition Workshops*. 1132–1142.
- Ronneberger, O., Fischer, P., and Brox, T., 2015. U-net: Convolutional networks for biomedical image segmentation. *In: Lecture Notes in Computer Science (including subseries Lecture Notes in Artificial Intelligence and Lecture Notes in Bioinformatics)*. Springer, Cham, 234–241.
- Sharifi, E., Saghafian, B., and Steinacker, R., 2019. Downscaling Satellite Precipitation Estimates With Multiple Linear Regression, Artificial Neural Networks, and Spline Interpolation Techniques. *Journal of Geophysical Research: Atmospheres*, 124 (2), 789–805.
- Singh, S. and Kansal, M.L., 2022. Chamoli flash-flood mapping and evaluation with a supervised classifier and NDWI thresholding using Sentinel-2 optical data in Google earth engine. *Earth Science Informatics*, 15 (2), 1073–1086.
- Sit, M., Seo, B.-C., and Demir, I., 2021. IowaRain: A Statewide Rain Event Dataset Based on Weather Radars and Quantitative Precipitation Estimation. arXiv preprint arXiv:2107.03432
- Sit, M., Seo, B.-C., and Demir, I., 2022. TempNet—Temporal Super Resolution of Radar Rainfall Products with Residual CNNs. EarthArxiv, 3606. <https://doi.org/10.31223/X5XS8R>
- Sivanpillai, R., Jacobs, K.M., Mattilio, C.M., and Piskorski, E. V., 2021. Rapid flood inundation mapping by differencing water indices from pre- and post-flood Landsat images. *Frontiers of Earth Science*, 15 (1), 1–11.
- Tiwari, V., Kumar, V., Matin, M.A., Thapa, A., Ellenburg, W.L., Gupta, N., and Thapa, S., 2020. Flood inundation mapping- Kerala 2018; Harnessing the power of SAR, automatic

- threshold detection method and Google Earth Engine. *PLOS ONE*, 15 (8), e0237324.
- Token, A., Kondmann, L., Weber, M., Eisenberger, M., Camero, A., Hu, J., Hoderlein, A.P., Şenaras, Ç., Davis, T., Cremers, D., Marchisio, G., Zhu, X.X., and Leal-Taixé, L., 2022. DynamicEarthNet: Daily Multi-Spectral Satellite Dataset for Semantic Change Segmentation.
- Twele, A., Cao, W., Plank, S., and Martinis, S., 2016. Sentinel-1-based flood mapping: a fully automated processing chain. *International Journal of Remote Sensing*, 37 (13), 2990–3004.
- Vandal, T.J., McDuff, D., Wang, W., Duffy, K., Michaelis, A., and Nemani, R.R., 2022. Spectral Synthesis for Geostationary Satellite-to-Satellite Translation. *IEEE Transactions on Geoscience and Remote Sensing*, 60.
- Wang, B., Sun, H., Cracknell, A.P., Deng, Y., Li, Q., Lin, L., Xu, Q., Ma, Y., Wang, W., and Zhang, Z., 2022. Detection and Quantification of Forest-Agriculture Ecotones Caused by Returning Farmland to Forest Program Using Unmanned Aircraft Imagery. *Diversity*, 14 (5), 406.
- Wang, J., Yang, X., Wang, Z., Cheng, H., Kang, J., Tang, H., Li, Y., Bian, Z., and Bai, Z., 2022. Consistency Analysis and Accuracy Assessment of Three Global Ten-Meter Land Cover Products in Rocky Desertification Region—A Case Study of Southwest China. *ISPRS International Journal of Geo-Information*, 11 (3), 202.
- Wickham, J., Stehman, S. V., Sorenson, D.G., Gass, L., and Dewitz, J.A., 2021. Thematic accuracy assessment of the NLCD 2016 land cover for the conterminous United States. *Remote Sensing of Environment*, 257, 112357.
- Wilson, L., van Dongen, R., Cowen, S., and Robinson, T.P., 2022. Mapping Restoration Activities on Dirk Hartog Island Using Remotely Piloted Aircraft Imagery. *Remote Sensing*, 14 (6), 1402.
- Xu, H., Demir, I., Koylu, C., and Muste, M., 2019. A web-based geovisual analytics platform for identifying potential contributors to culvert sedimentation. *Science of the Total Environment*, 692, 806–817.
- Yang, Q., Shen, X., Anagnostou, E.N., Mo, C., Eggleston, J.R., and Kettner, A.J., 2021. A High-Resolution Flood Inundation Archive (2016–the Present) from Sentinel-1 SAR Imagery over CONUS. *Bulletin of the American Meteorological Society*, 102 (5), E1064–E1079.
- Yang, Z., Diao, C., and Li, B., 2021. A robust hybrid deep learning model for spatiotemporal image fusion. *Remote Sensing*, 13 (24), 5005.
- Yildirim, E. and Demir, I., 2022. Agricultural flood vulnerability assessment and risk quantification in Iowa. *Science of The Total Environment*, 826, 154165.
- Zanaga, D., Van De Kerchove, R., De Keersmaecker, W., Souverijns, N., Brockmann, C., Quast, R., Wevers, J., Grosu, A., Paccini, A., Vergnaud, S., Cartus, O., Santoro, M., Fritz, S., Georgieva, I., Lesiv, M., Carter, S., Herold, M., Linlin, L., Tsendbazar, N., Raimoino, F., and Arino, O., 2021. ESA WorldCover 10 m 2020 v100. *Meteosat Second Generation Evapotranspiration (MET)*, 1–27.
- Zeng, Z., Gan, Y., Kettner, A.J., Yang, Q., Zeng, C., Brakenridge, G.R., and Hong, Y., 2020. Towards high resolution flood monitoring: An integrated methodology using passive microwave brightness temperatures and Sentinel synthetic aperture radar imagery. *Journal of Hydrology*, 582, 124377.
- Zhang, M., Chen, F., Liang, D., Tian, B., and Yang, A., 2020. Use of sentinel-1 grd sar images to delineate flood extent in Pakistan. *Sustainability (Switzerland)*, 12 (14), 1–19.
- Zheng, Z., Zhong, Y., Wang, J., and Ma, A., 2020. Foreground-Aware Relation Network for

Geospatial Object Segmentation in High Spatial Resolution Remote Sensing Imagery. *In: Proceedings of the IEEE Computer Society Conference on Computer Vision and Pattern Recognition*. 4095–4104.

Zhu, J. and Kelly, T., 2021. Seamless Satellite-image Synthesis. *Computer Graphics Forum*, 40 (7), 193–204.